AIAA JOURNAL
Vol. 49, No. 12, December 2011

High-Resolution Numerical Method for Supercritical Flows with Large Density Variations

Hiroshi Terashima*
Japan Aerospace Exploration Agency, Tsukuba, Ibaraki 305-8505, Japan
Soshi Kawai†
Stanford University, Stanford, California 94305
and
Nobuhiro Yamanishi‡
Japan Aerospace Exploration Agency, Tsukuba, Ibaraki 305-8505, Japan

DOI: 10.2514/1.J051079

A high-resolution methodology using a high-order compact differencing scheme with localized artificial diffusivity is introduced with the aim of simulating jet mixing under supercritical pressure environments. The nonlinear localized artificial diffusivity provides the stability to capture different types of discontinuity, such as shock wave, contact surface, and material interface, whereas the high-order compact difference scheme resolves broadband scales in the rest of the domain. The present method is tested on several one-dimensional discontinuity-related problems under super/transcritical conditions and a comparatively more illustrative two-dimensional low-temperature planar jet problem under a supercritical pressure condition. The localized artificial diffusivity, especially artificial thermal conductivity for temperature gradients, effectively suppresses numerical wiggles near the interfaces. The effects of the artificial thermal conductivity on numerical stability and accuracy are examined. Comparisons between the present method and a conventional low-order scheme demonstrate the superior performance of the present method for resolving a wide range of flow scales while successfully capturing large density/temperature variations at interfaces.

I. Introduction

AN UNDERSTANDING of the thermo-fluid dynamics related to the injection of cryogenic propellant in high pressure conditions is essential in the design and performance of liquid rocket engines [1]. The latest engines are required to operate at high chamber pressures ranging from approximately 3 MPa to typically 10–20 MPa to achieve high thrust performance. These conditions typically exceed the critical point of a particular propellant, i.e., the supercritical thermodynamic conditions. In such environments, an injected propellant exhibits unique behavior. For example, near the critical point, the constant pressure specific heat increases rapidly, and large expansions of the fluid occur with small increases in temperature. The surface tension and latent heat tend to decrease with increasing pressure. These unique phenomena do not appear in ideal flow conditions, indicating that propellant injection under supercritical thermodynamic conditions is fundamentally different from that under subcritical pressure conditions and largely unknown. We are, therefore, interested in exploring the physics of cryogenic jet flows injected into supercritical pressure conditions; such a study may shed light on other related physics, such as combustion instabilities.

Generally, it is considered that gas-like mixing, rather than atomization processes, dominates the mixing process in supercritical pressure conditions because of the lack of surface tension and disappearance of the latent heat in such conditions [1–3]. A pioneering work in numerical simulations was done by Oefelein and Yang [4] for the two-dimensional (2-D) large-eddy simulation (LES) of supercritical mixing and combustion where spatial discretization was obtained using a fourth-order flux-differencing scheme and a total-variation-diminishing (TVD) scheme. Meng and Yang [5] presented a unified treatment based on general fluid thermodynamics for supercritical flow simulations. Zong et al. [6,7] numerically investigated the evolution of a cryogenic fluid jet under supercritical conditions by means of LES. In these studies [5,6], a fourth-order central differencing scheme was employed with fourth-order scalar dissipation to ensure computational stability and prevent numerical oscillations. Hosangadi et al. [8] simulated a supercritical coaxial jet flow using a hybrid Reynolds-averaged Navier-Stokes (RANS)/LES methodology where a second-order numerical flux was used on an unstructured grid. Schmitt et al. [9] recently carried out LES of supercritical pressure round jets. They employed a Taylor-Galerkin third-order scheme on an unstructured grid, adding a sensor-based dissipation procedure for computational stabilization. RANS simulations were also performed for supercritical jet flows [10,11] where unsteady features of jet flow were mostly absent.

Bellan [12], Miller et al. [13], and Okong'o and Bellan [14] employed direct numerical simulation (DNS) for temporal mixing layers at supercritical pressure conditions using an eighth-order central finite differencing scheme or a sixth-order compact differencing scheme. Selle et al. [15] and Taskinoglu and Bellan [16] subsequently conducted LES of binary-species temporal mixtures to analyze and develop subgrid-scale models for LES using previously produced DNS data. Selle and Schmitt [17] simulated homogeneous isotropic turbulence under a supercritical pressure condition using an eighth-order finite-difference scheme. Comprehensive reviews on supercritical mixing and combustion can be found in Yang [18] and Bellan [12], respectively.

Received 17 November 2010; revision received 16 May 2011; accepted for publication 20 May 2011.

*Project Researcher, JAXA's Engineering Digital Innovation Center, 2-1-1 Sengen; currently Project Assistant Professor, University of Tokyo, Tokyo 113-8656, Japan; htera@rocketlab.t.u-tokyo.ac.jp. Member AIAA (Corresponding Author).

†Post-Doctoral Fellow, Center for Turbulence Research, 488 Escondido Mall; currently JAXA International Top Young Fellow, the Institute of Space and Astronautical Science, Japan Aerospace Exploration Agency, Sagamihara, Kanagawa 252-5210, Japan. Senior Member AIAA.

‡Senior Engineer, JAXA's Engineering Digital Innovation Center, 2-1-1 Sengen. Member AIAA.

As mentioned, except for the simple mixing layer computations by Bellan [12], Miller et al. [13], and Okong'o and Bellan [14] and isotropic turbulence simulations by Selle and Schmitt [17], lower-order spatial schemes, coupled with artificial dissipation terms, have been employed in most of the LES simulations related to supercritical jet flows. This was done to avoid possible numerical instabilities due to the existing large density/temperature gradients. Thus, the differencing errors (both dispersion and dissipation) in the numerical schemes used so far are possibly too large to accurately resolve the broad range of turbulence scales and the interactions between turbulence and supercritical thermodynamic properties. On the other hand, the application of high-order and, preferably, high-resolution schemes based on central differencing methods to supercritical low-temperature jet flows is a challenging issue because of the existence of large density/temperature gradients in the flowfields. A key issue here is to suppress possible spurious oscillations while minimizing its influence on resolved broadband scales of flow motions using high-order/resolution schemes. It should also be mentioned that several studies [19–21] using the ideal gas law have demonstrated that the numerical dissipation in high-order upwind-biased schemes, such as weighted essentially nonoscillatory (WENO) schemes [22], overwhelms a wide range of scales of turbulence, even if the formal order of accuracy is high. A latest review [23] also indicated that WENO-typed schemes are quite computationally intensive and suffer from numerical damping in smooth zones of the flowfield.

In this study, we present a simple yet efficient high-resolution numerical method for simulations of supercritical flows with large density/temperature gradients. This method uses a sixth-order compact differencing scheme to resolve broadband scales of flow motions in smooth regions, although nonlinear localized artificial diffusivity (LAD) is introduced to capture large density/temperature variations near interfaces and shocks. This study builds on our previous work [24] and extends it to supercritical flows. The present study focuses on demonstrating the performance of the proposed method and its applicability to supercritical flows with large density/temperature gradients, aiming to develop future applications of the method to LES of supercritical jet flows. Several one-dimensional (1-D) inviscid problems were considered, and a 2-D viscous supercritical jet simulation was carried out. An advection problem and a modified Shu-Osher problem are proposed to investigate the performance of the present method in supercritical conditions. Although only single-species flows, such as those typically investigated experimentally and numerically in the literature [6,9,25,26], are considered in this study, the extension to multispecies flows is straightforward. We have, in a previous study [24], shown the multispecies capability of the method in ideal gas law conditions.

II. Numerical Methodology

A. Governing Equations

The compressible Euler/Navier-Stokes equations are used as the governing equations:

$$\frac{\partial \rho}{\partial t} + \nabla \cdot (\rho \boldsymbol{u}) = 0 \tag{1}$$

$$\frac{\partial \rho \boldsymbol{u}}{\partial t} + \nabla \cdot (\rho \boldsymbol{u}\boldsymbol{u} + p\boldsymbol{I} - \boldsymbol{\tau}) = 0 \tag{2}$$

and

$$\frac{\partial E}{\partial t} + \nabla \cdot (E\boldsymbol{u} + p\boldsymbol{I} \cdot \boldsymbol{u} - \boldsymbol{\tau} \cdot \boldsymbol{u} - \kappa \nabla T) = 0 \tag{3}$$

Here, ρ is the density, $\boldsymbol{u}$ the velocity vector, p the static pressure, E the total energy, T the temperature, $\boldsymbol{\tau}$ the viscous stress tensor, $\boldsymbol{I}$ the unit tensor, and κ the thermal conductivity. The viscous stress tensor $\boldsymbol{\tau}$ is given as

$$\boldsymbol{\tau} = \mu(2\boldsymbol{S}) + \left(\beta - \frac{2}{3}\mu\right)(\nabla \cdot \boldsymbol{u})\boldsymbol{I}, \qquad \boldsymbol{S} = \frac{1}{2}(\nabla \boldsymbol{u} + (\nabla \boldsymbol{u})^T) \tag{4}$$

where μ is the dynamic viscosity, β the bulk viscosity, and $\boldsymbol{S}$ the strain rate tensor.

To close the governing equations and evaluate the fluid properties under supercritical conditions, the Soave-Redlich-Kwong (SRK) equation of state [27] is applied. The SRK equation of state is written as

$$p = \frac{RT}{V - b} - \frac{a\alpha}{V^2 + bV} \tag{5}$$

where R is the specific gas constant, and the constant parameters $a = 0.4275R^2T_{\mathrm{cr}}^2/p_{\mathrm{cr}}$ and $b = 0.0866RT_{\mathrm{cr}}/p_{\mathrm{cr}}$ represent the intermolecular interaction and the effective volume of molecules, respectively; the subscript cr denotes the critical point. α is a function of the temperature and the acentric factor given in Appendix A. $V(=1/\rho)$ is the volume per unit mass. The cubic equations of state, such as those of the SRK model, describe thermodynamic behavior in a wide range of conditions and are computationally efficient compared with more complex equations of state, such as the Benedict-Webb-Rubin (BWR) equation of state [28,29].

Considering thermodynamic relationships, the internal energy is expressed as

$$\begin{aligned} e(T, \rho) &= \int \left(\frac{\partial e}{\partial T}\right)_V \mathrm{d}T + \int \left(\frac{\partial e}{\partial V}\right)_T \mathrm{d}V \\ &= e_0(T) + \int_\infty^V \left[T\left(\frac{\partial p}{\partial T}\right)_V - p\right]_T \mathrm{d}V \end{aligned} \tag{6}$$

where $e_0(T)$ is the reference internal energy for a thermally perfect gas, and the second term is the departure function, which is defined as the difference between perfect and real fluid properties. As the density and the internal energy are independent variables, the temperature is solved using an equation obtained from Eqs. (5) and (6). The pressure is then calculated with Eq. (5). For the 2-D viscous flow computations, the dynamic viscosity is calculated using the model of Zeberg-Mikkelsen et al. [30], and the thermal conductivity is calculated using the model of Vasserman and Neodostup [31]. Detailed descriptions of the thermodynamic fluid properties are given in Appendix A.

B. Spatial Differencing and Temporal Integration

The spatial derivatives in the governing Eqs. (1–3) are evaluated using a sixth-order compact differencing scheme [32]. Temporal integration is achieved by using a third-order TVD Runge-Kutta scheme [33]. A sixth-order low-pass spatial filtering scheme [32,34] is applied to the conservative variables once in each direction after the final stage of the Runge-Kutta scheme for computational stability; for this, a free parameter α_f is fixed to $\alpha_f = 0.495$. We note that, as demonstrated later, the order of accuracy of the present method is little influenced by the order of the filtering scheme (sixth- or eighth-order). Detailed descriptions of the sixth-order compact differencing scheme and the filtering scheme, including the boundary treatments, are given in Appendix B.

C. Localized Artificial Diffusivity Method

Central differencing schemes, including the compact differencing scheme used in this study, produce nonphysical spurious oscillations if flows involve numerical discontinuities due to, e.g., shock waves or interfaces. In supercritical pressure conditions, although a phase equilibrium no longer exists (no property jump across the interface), there are still physical jumps at fluid interfaces, e.g., when considering a situation wherein a cryogenic jet is injected into a room temperature environment. Figure 1, for example, presents a thermodynamic property of nitrogen at a supercritical pressure, 4 MPa using the SRK and the ideal gas equations of state. The density varies significantly with temperature within a very narrow range across the pseudocritical temperature, resulting in a strong density gradient against temperature, which cannot be seen with the ideal gas model.

A key issue is to suppress possible nonphysical spurious oscillations without affecting resolved flow motions. Selle and Schmitt

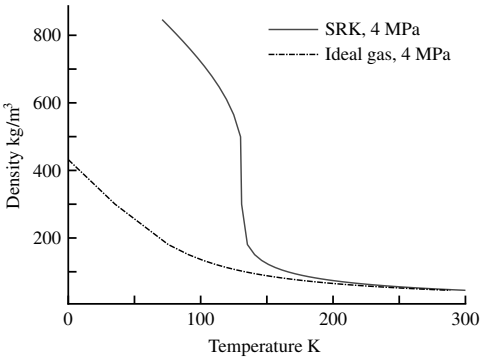

Fig. 1 Thermodynamic property of nitrogen: a T-ρ diagram with comparison of equation of state.

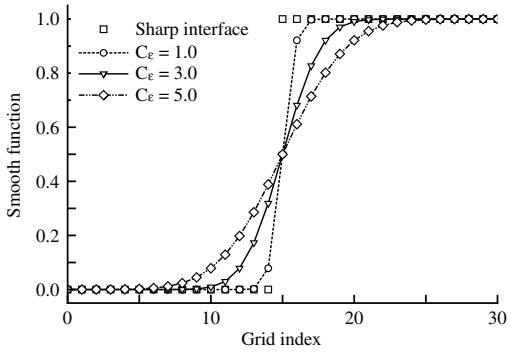

Fig. 2 Profiles of sharp and three smooth initial interfaces.

[17] used an artificial stabilization procedure [35] to overcome the large density gradients encountered under supercritical pressure conditions. Zong et al. [6,7] also used such a scalar dissipation technique using a fourth-order central differencing scheme. In this study, we adopt a strategy to add nonlinear artificial fluid transport coefficients to the physical fluid transport coefficients in the Navier-Stokes Eqs. (1–3) proposed by Cook and Cabot [36] and Cook [37] as follows:

$$\mu = \mu_f + \mu^* \tag{7}$$

$$\beta = \beta_f + \beta^* \tag{8}$$

and

$$\kappa = \kappa_f + \kappa^* \tag{9}$$

where the subscript f and superscript $*$ denote the physical and artificial fluid transport coefficients, respectively.

β_f is set to be zero due to the Stokes' hypothesis. As the present applications are limited to one- and 2-D problems, the artificial viscosity μ^* is not introduced. The artificial bulk viscosity β^* is considered only in those cases in which a shock wave appears in the flowfields (defined later). The key aspect of the LAD method in this study is to introduce the artificial thermal conductivity κ^* in order to handle large density/temperature gradients at interfaces. κ^* is modeled in the generalized form by Kawai et al. [21] using the derivative of temperature proposed by Cook [38] as

$$\kappa^* = C_\kappa \overline{\frac{\rho c_s^3}{T^2}\left|\sum_{l=1}^{n_d}\frac{\partial^r T}{\partial \xi_l^r}\Delta\xi_l^r \Delta_l\right|} \tag{10}$$

where c_s is the speed of sound in real fluids and n_d (= 1–3) is the number of dimensions. C_κ is a dimensionless user-specified constant. ξ_l refers to generalized curvilinear coordinates ξ, η, and ζ, when l is 1, 2, and 3, respectively. $\Delta\xi_l$ is the grid spacing in generalized curvilinear coordinates, usually set to $\Delta\xi_l = 1$. Δ_l is the grid spacing in physical space, defined as $\Delta_l = (x_{l+1} - x_{l-1})/2$. The order of derivative r in Eq. (10) is taken to be sufficiently large, $r = 4$, so that the artificial transport coefficients are localized in the regions of shock wave, contact discontinuity, and material interface and vanish automatically in well-resolved regions. Thus, the artificial properties are designed to smooth out the discontinuities sufficiently such that they can be resolved by the central differencing scheme. The fourth-derivative terms are evaluated using an explicit fourth-order central differencing scheme [32]. The over-bar in Eq. (10) denotes an approximate truncated-Gaussian filter [36] for removal of the cusps generated by high-order derivative operators. The discretization related to the LAD method is given in Appendix B. The performance of the LAD method was thoroughly examined under the ideal gas law [21,39].

Because all the earlier works related to the LAD method were carried out assuming the ideal gas law, the performance of the dimensionless user-specified constants for real fluid environments is still unproven. The performance of κ^* is, therefore, investigated through a 1-D interface advection problem to determine an optimal value of the user-defined constant C_κ. The default value, $C_\kappa = 0.01$, obtained from earlier studies [37,39], is used unless otherwise stated.

The advantages of the present method are its high-resolution characteristics, simple formulation, ease of implementation, and absence of weighting/hybrid procedures as compared with existing high-order discontinuity-capturing schemes (e.g., high-order WENO schemes [22] and hybrid central differencing/shock-capturing schemes [40,41]). The LAD method can localize artificial dissipation in regions where unresolved high wave number fluctuations exist, whereas the high-resolution characteristics of a high-order compact differencing scheme are preserved in smooth regions; these are desirable characteristics of numerical schemes for LES and DNS.

D. Smooth Initial Interface

Our previous study [24] demonstrated that the use of a smooth initial interface is effective for avoiding initial startup error [42]. The smooth initial interface is generated by using the error function $\mathrm{erf}(x)$ and primitive variables $q = (\rho, \boldsymbol{u}, p)$:

$$q = q_L(1 - f_{\mathrm{sm}}) + q_R f_{\mathrm{sm}}, \qquad f_{\mathrm{sm}} = \frac{(1 + \mathrm{erf}[\Delta R/\epsilon])}{2} \tag{11}$$

Here, the subscripts L/R denote the left and right statuses, ΔR is the distance from the initial interface, and ϵ is defined as $\epsilon = C_\epsilon \Delta x$, where Δx is the grid spacing. C_ϵ is a free parameter for adjusting the smoothness of the initial interface. As C_ϵ increases, the initial interface spreads over more grid points, as shown in Fig. 2. Note that, once C_ϵ is fixed, the initial interface is represented with the same number of grid points even if the total number of grid points is changed.

III. Results

A. One-Dimensional Cases

All the computations in 1-D inviscid cases are conducted with the Courant-Friedrichs-Lewy (CFL) number = 0.4 and uniform grid spacing. Nitrogen is considered as the working fluid, except for the shock tube problem. The critical temperature, pressure, and density of nitrogen are $T_{\mathrm{cr,N_2}} = 126.2$ K, $p_{\mathrm{cr,N_2}} = 3.4$ MPa, and $\rho_{\mathrm{cr,N_2}} = 313.3$ kg/m^3, respectively [43].

1. *Interface Advection Problem*

An interface advection problem under supercritical pressure condition is introduced as the first test case to assess the capability of the present method. The effects of the smooth initial interface and the artificial transport coefficient κ^* are investigated. Based on the experimental conditions for a cryogenic jet injected into supercritical pressures [3,44], the initial conditions are set to be

$$(\rho, u, p, T) = \begin{cases} (450.0\,\mathrm{kg/m^3}, 10.0\,\mathrm{m/s}, 4.0\,\mathrm{MPa}, 124.6\,\mathrm{K}) & \text{if } 0.0 \le x \le 0.3\,\mathrm{m}, \\ (45.0\,\mathrm{kg/m^3}, 10.0\,\mathrm{m/s}, 4.0\,\mathrm{MPa}, 298.5\,\mathrm{K}) & \text{if } 0.3 < x \le 1.0\,\mathrm{m} \end{cases} \tag{12}$$

Here, the initial conditions are designed such that the transcritical state, where the temperature exceeds the critical temperature, can be seen across the interface. Such transcritical mixing behavior is a unique physical phenomenon observed in liquid rocket engines [1]. Note that the temperature is estimated from the specified density and pressure using the SRK equation of state, which may be varied for different equations of state. The computations are performed using 101 grid points with a grid spacing of $\Delta x = 0.01$, and the results presented are those at $t = 0.04$ s unless otherwise stated. The constant $C_\kappa = 0.01$ is used as the default value. $\rho_{\mathrm{ref}} = 450.0$ kg/m^3, $u_{\mathrm{ref}} = 10.0$ m/s, $p_{\mathrm{ref}} = 4.0$ MPa, and $T_{\mathrm{ref}} = 124.6$ K are used for normalization in several figures.

First, it is worth noting that computations without the LAD method failed (a sharp initial interface and $C_\epsilon = 1.0$) or produced significant wiggles (the other smooth initial interfaces), even when lower values of the free parameter in the filtering scheme, such as $\alpha_f = 0.4$ or 0.45, were used. This fact suggests that the smooth initial interface (e.g., $C_\epsilon = 3$) still maintains the large gradient, which cannot be handled by simply strengthening the filtering and needs to be captured by some discontinuity-capturing methods. We also found that lowering free parameters adversely produces larger spurious oscillations. More important, because the free parameter strongly influences on flowfields, especially turbulence transition phenomena [45], lowering the value should be avoided.

a. Effect of Smooth Initial Interface. Figure 3 shows the profiles of density, velocity, pressure, and temperature at $t = 0.04$ s with different smoothness in the initial profile. In the profiles of density and temperature, the sharp and smooth ($C_\epsilon = 1.0$) initial interfaces generate small wiggles near the interface because of the initial startup error, whereas for the other smooth initial interfaces ($C_\epsilon = 3.0$ and 5.0) the profiles are smooth without any significant spurious oscillations. The results with $C_\epsilon = 3.0$ and 5.0 are in good agreement with the exact solutions (although the exact profile is plotted only for $C_\epsilon = 3.0$). Spurious oscillations are seen in the profiles of velocity and pressure with the sharp and smooth ($C_\epsilon = 1.0$) initial interfaces; however, the magnitudes are quite

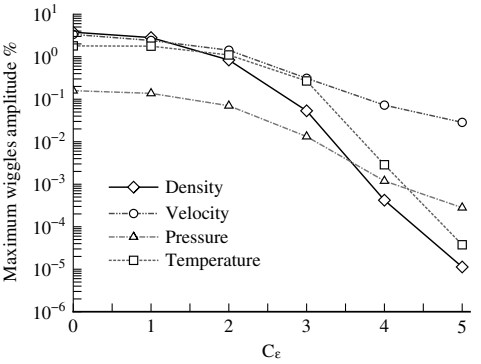

Fig. 4 Maximum wiggles amplitudes at $t = 0.04$ s.

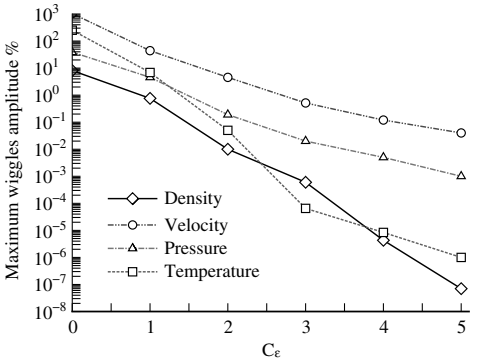

Fig. 5 Maximum wiggles amplitudes in the initial stage (at $t \approx 2.15 \times 10^{-4}$ s).

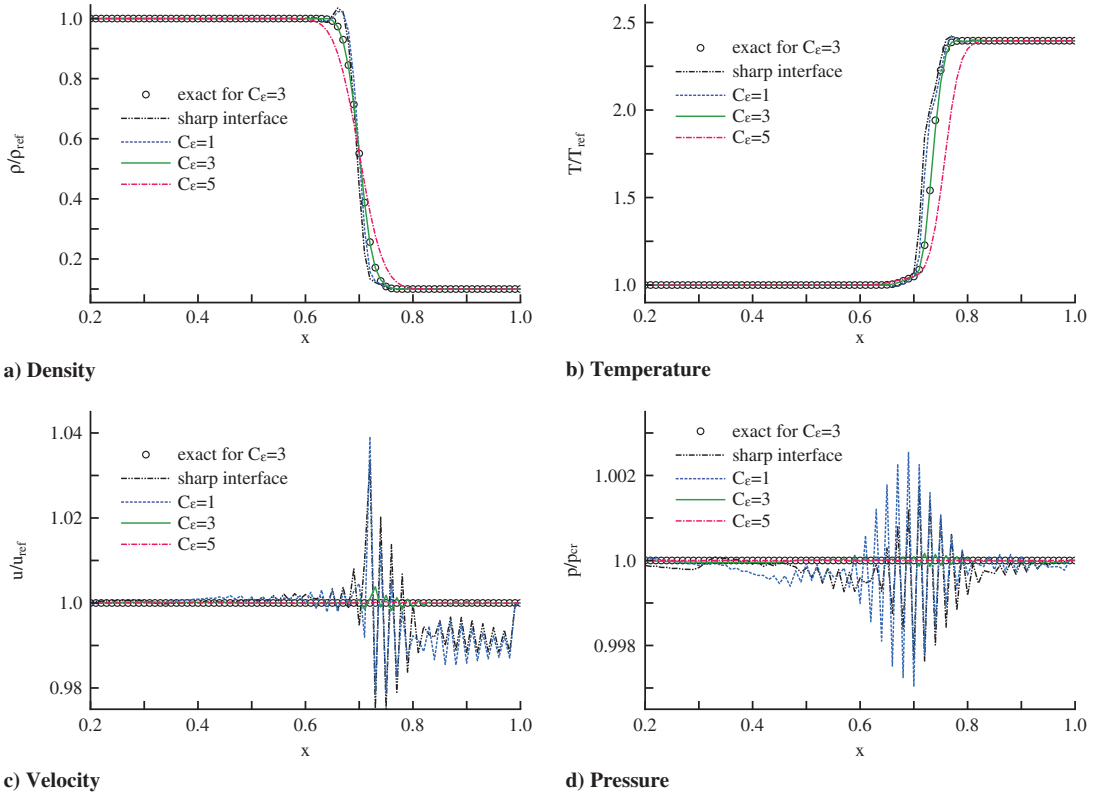

Fig. 3 Profiles at $t = 0.04$ s with the effect of initial interfaces.

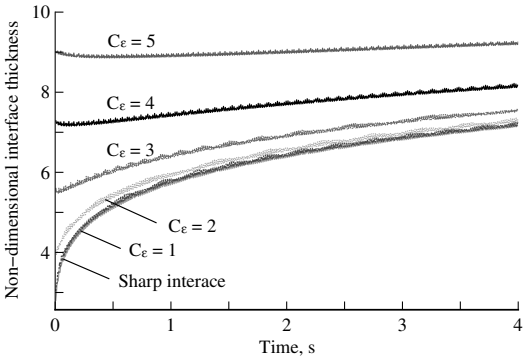

Fig. 6 Time histories of nondimensional interface thickness using density profile.

small. The magnitudes of spurious oscillation are reduced for larger values of C_ϵ. For example, the maximum wiggles amplitude (defined as the maximum difference between the exact (analytical) and the computed profiles) of velocity and pressure with $C_\epsilon = 3.0$ are approximately 0.4% and 0.01%, respectively. Figure 4 summarizes the maximum wiggles amplitudes of four primitive variables for different values of C_ϵ. It shows that the smooth initial interface can effectively reduce the wiggles amplitudes, which are all less than 0.4% for $C_\epsilon = 3.0$. Figure 5 shows the maximum wiggles amplitude estimated during the first 20 steps ($t \approx 2.15 \times 10^{-4}$ s). As compared with the results at $t = 0.04$ s (Fig. 4), the wiggles produced in the initial stage are quite large, especially for the sharper initial interfaces. For example, the maximum wiggles amplitude for velocity is 1042.9% for the sharp initial interface and 44.1% for $C_\epsilon = 1.0$. The amplitudes rapidly reduce with increasing C_ϵ. Therefore, the smooth initial interface effectively works to avoid the numerical instability in the initial stage. Note that, as mentioned previously, the interface is represented by a constant number of grid points even if the total number of grid points is increased with fixed C_ϵ (i.e., in other words, the initial interface becomes thinner in physical space when the grid resolution is increased with fixed C_ϵ). Hence, the increase in the grid resolution with fixed C_ϵ does not affect the amplitude of resultant wiggles but their frequency. Almost identical results were obtained in the case of 8 MPa (although not shown here).

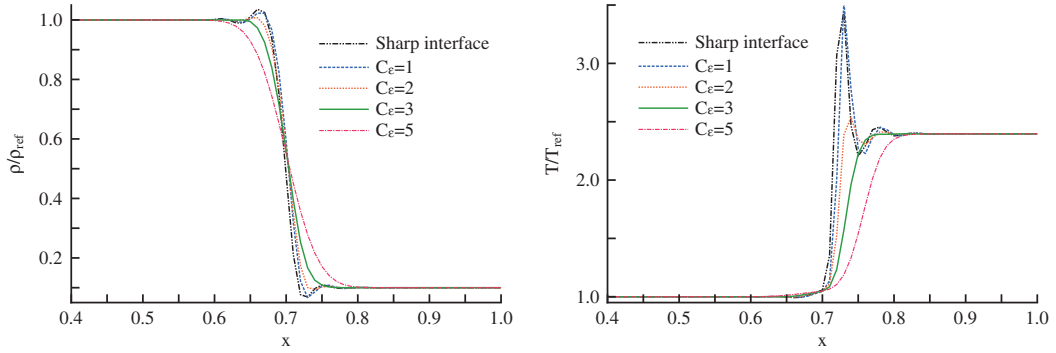

Fig. 7 Density and temperature profiles at $t = 0.04$ s with a small user-specified constant $C_\kappa = 0.001$ with the effect of initial interface.

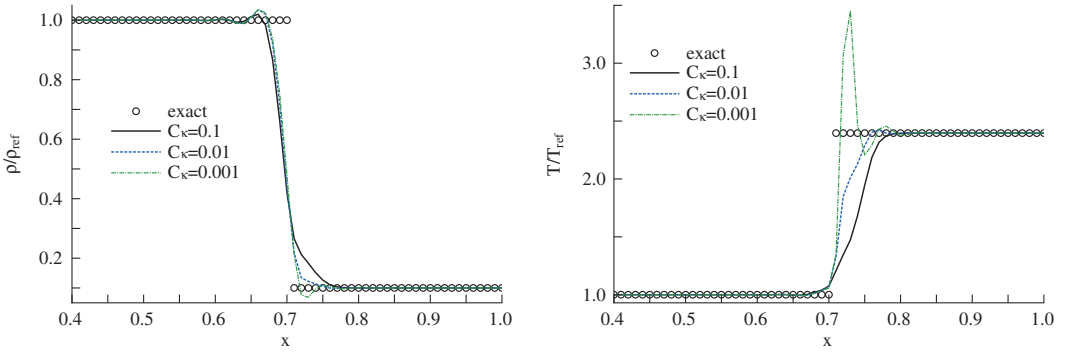

a) Sharp interface

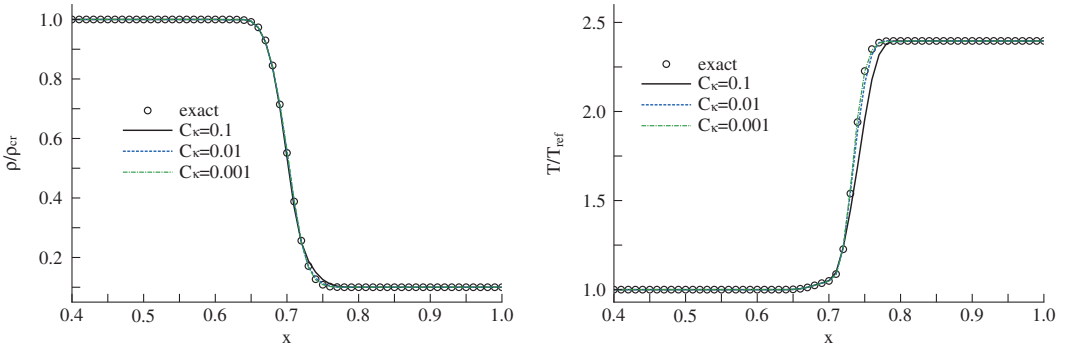

b) Smooth initial interface $C_\epsilon = 3.0$

Fig. 8 Effect of the user-specified constant C_κ for the artificial thermal conductivity κ^*. Density (left) and temperature (right).

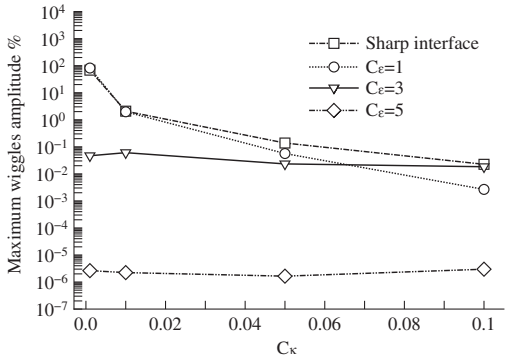

a) Maximum wiggles amplitude

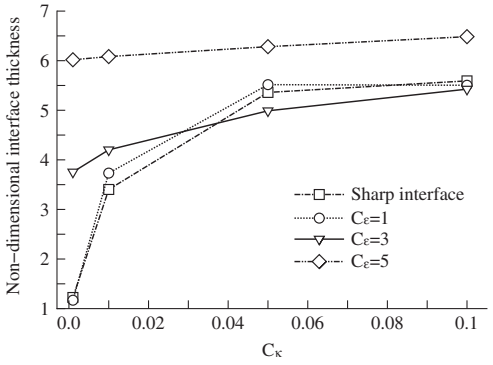

b) Nondimensional interface thickness

Fig. 9 Effect of C_κ using temperature profiles at $t = 0.04$ s.

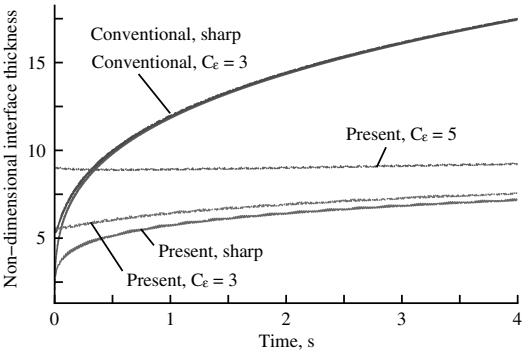

Fig. 11 Time histories of nondimensional interface thickness: comparison between the present method and the conventional low-order scheme.

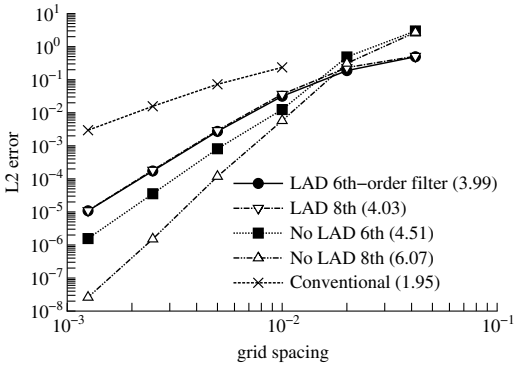

Fig. 12 Order of accuracy with the advection problem.

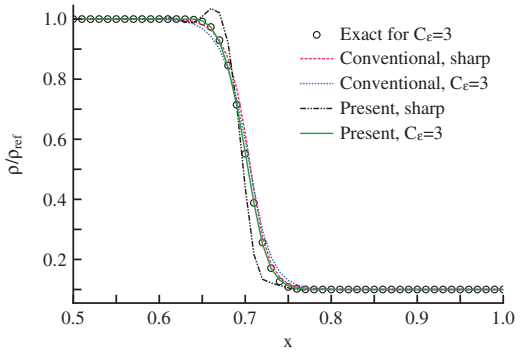

a) Density

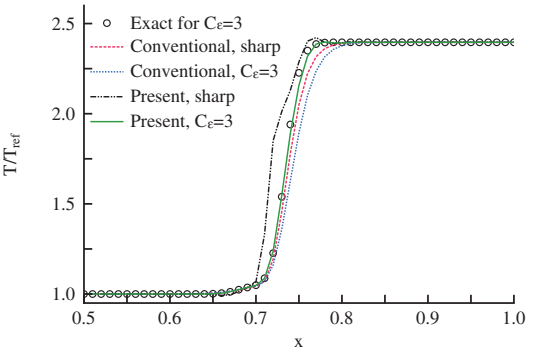

b) Temperature

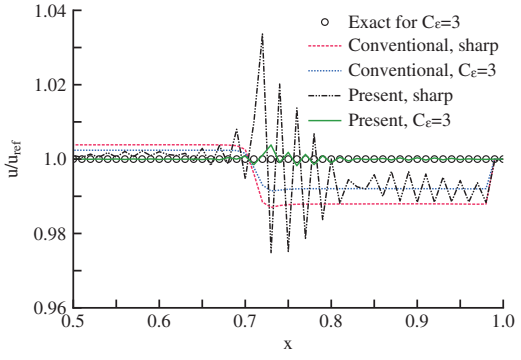

c) Velocity

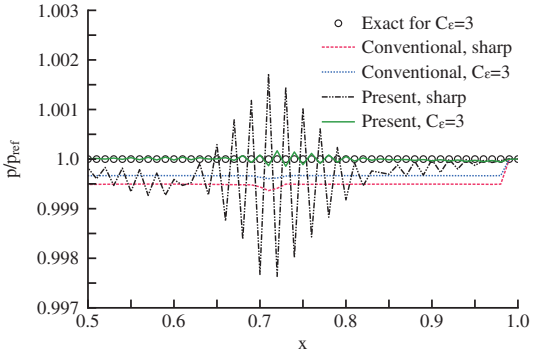

d) Pressure

Fig. 10 Profiles at $t = 0.04$ s with comparison between the present method and the conventional low-order scheme (SHUS with MUSCL).

Figure 6 presents the time histories of nondimensional interface thickness δ using the density profile, which is defined as

$$\frac{\delta}{\Delta x} = \frac{\Delta\rho}{\Delta x \partial\rho/\partial x|_{\max}} \tag{13}$$

where $\Delta\rho = \rho_L - \rho_R$ and Δx are the grid spacing. The simulation was run until $t = 4.0$ s, which is a significantly long period, to make the dissipation characteristics clear. A longer domain and the same mesh resolution ($\Delta x = 0.01$) is used. In case of the sharper initial interfaces, the interface thickness diffuses rapidly until $t < 0.5$ s, whereas with larger C_ϵ it is almost constant during the computations. All the interfaces eventually have almost the same rate of variations, and their thicknesses remain nearly unchanged.

b. Effect of Artificial Thermal Conductivity κ^*. Figure 7 shows the density and temperature profiles for a small user-specified constant $C_\kappa = 0.001$. By comparing these results with those of the default value $C_\kappa = 0.01$ (Fig. 3), it is seen that large wiggles appear in the temperature profile when sharper initial interfaces are used, whereas the density profiles show no significant effect of κ^*. These results, therefore, indicate that κ^* successfully suppresses spurious oscillations, especially those that appear in the temperature profile. In the case of smaller C_κ, the smooth initial interface with $C_\epsilon = 2$ still produces visible wiggles at the interface, indicating $C_\epsilon \geq 3$ may be preferable.

Figure 8 shows the effect of the user-specified constant C_κ on the density and temperature profiles in cases of the sharp and smooth ($C_\epsilon = 3.0$) initial interfaces. Although the wiggles are significantly reduced by increasing C_κ, the shape of the profile is unfavorably smoothened, which eventually disagrees with the exact profiles (see the temperature profiles with $C_\kappa = 0.1$). Although not shown here, the velocity and pressure profiles show that increasing C_κ reduces the amplitude of the wiggles but has little influence on the frequency. Figure 9 shows the maximum wiggles amplitude and the nondimensional interface thickness using the temperature profiles for different values of C_κ. There is a clear trade-off between the wiggles amplitude and the interface thickness. As C_κ increases, the interface is smeared, and the wiggles amplitude decreases. Although the value of C_κ is set depending on the users, this analysis shows that $C_\kappa = 0.01$ reduces the wiggles amplitude even for sharp initial interfaces (2.0% with $C_\kappa = 0.01$ and 68% with $C_\kappa = 0.001$) while maintaining reasonable interface thickness. Thus, $C_\kappa = 0.01$ is used for all the test

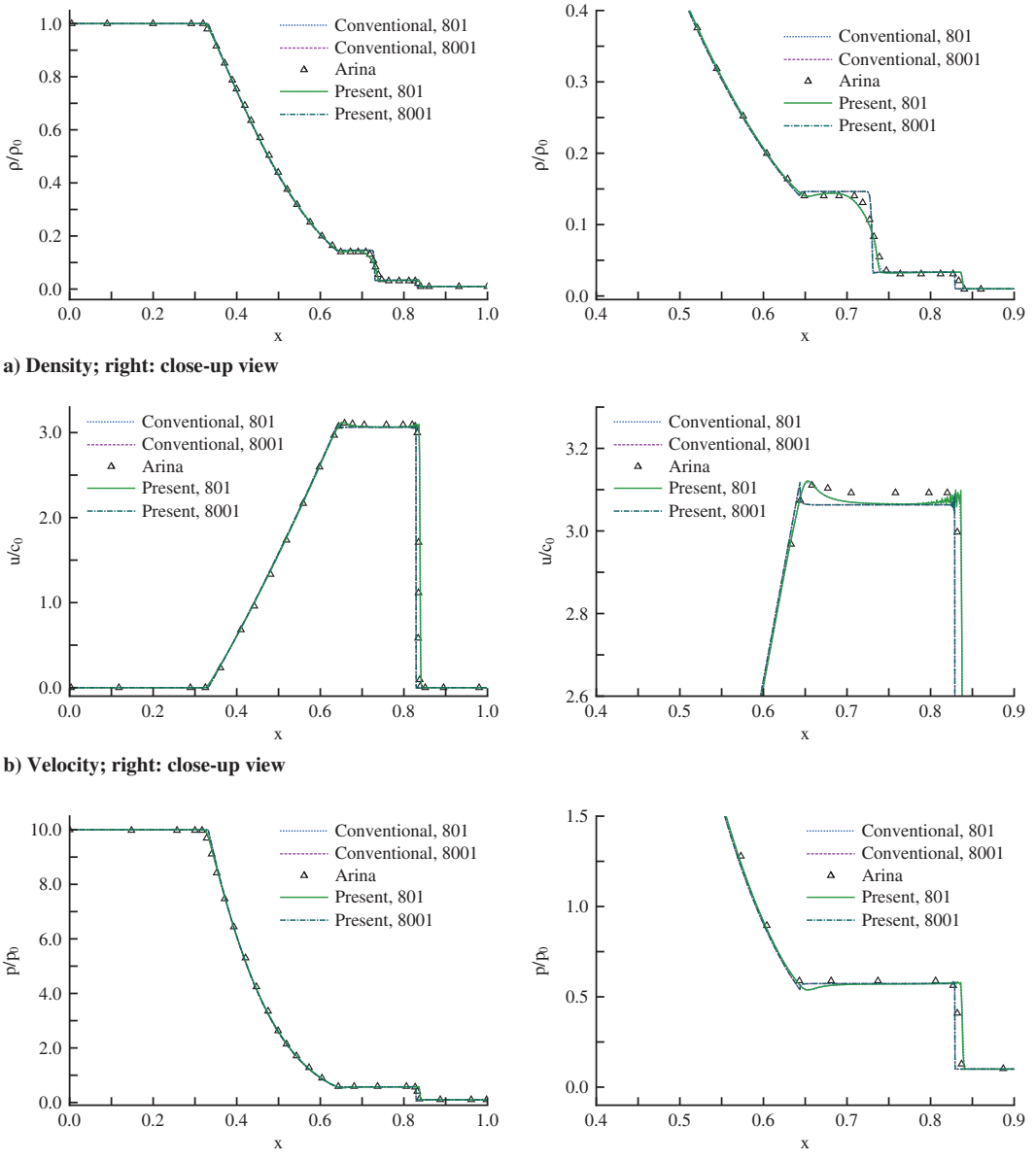

a) Density; right: close-up view

b) Velocity; right: close-up view

c) Pressure; right: close-up view

Fig. 13 Comparisons with the conventional low-order scheme and an earlier work (Arina) [55]. Here, c_0 is simply estimated by $c_0 = \sqrt{\gamma_0 p_0/\rho_0}$, where γ_0 is 1.3 for carbon dioxide.

cases discussed in the rest of the paper. It should be noted that, without the addition of κ^*, computations using sharper interfaces failed.

c. Comparison with a Conventional Low-Order Scheme. Conventional low-order upwind-biased schemes, because of their robustness, have been successfully and widely used for solving the compressible Navier-Stokes equations, including multicomponent flows [8,46–48]. We, therefore, compared the performance of our method with that of a conventional low-order scheme. For this purpose, we used the simple high-resolution upwind scheme (SHUS) [49], which belongs to the family of the advection upstream splitting method (AUSM) scheme [50]) with the third-order monotone upwind scheme for conservation law (MUSCL) interpolation [51,52] and the van Albada limiter [53]. The conventional scheme has third-order spatial accuracy. Computations were conducted with the same mesh resolution ($\Delta x = 0.01$) and the same CFL number (CFL $= 0.4$).

Figure 10 shows the profiles of density, temperature, velocity, and pressure. As expected, because of its dissipative nature, the conventional low-order scheme does not produce any spurious oscillations even for the sharp initial interface and in the first few steps. However, the velocity and pressure profiles obtained by the conventional scheme show small bumps near the interface, indicating the conventional scheme is unable to maintain the velocity and pressure equilibrium across the interface because of the different thermodynamic fluid properties, a well-known problem when the conservative form is used for compressible multicomponent flows [54]. On the other hand, the present method with $C_\epsilon = 3.0$ almost maintains the velocity and pressure equilibrium across the interface, whereas the sharp initial interface shows oscillatory results near the interface.

The time history of interface thickness with Eq. (13) is shown in Fig. 11 using the density profiles. The interface thicknesses with the conventional scheme grow at a faster rate because of its excessive dissipation characteristics. The present method clearly keeps the interfaces much sharper than those of the conventional scheme, which demonstrates the low dissipation characteristics of the present method. It should be noted that the computation using the conventional scheme with the sharp initial interface failed without the limiter function.

The computational cost of the present method is quite comparable to that of the conventional scheme based on counting the four arithmetic operations required to compute the convective terms. Further, the two references [20,24] estimated that the computational costs of the present numerical framework requires roughly less than $1/3$ and $1/6$ of the computational costs required for the fifth- and the seventh-order WENO schemes.

d. Order of Accuracy. An analysis of the order of accuracy is provided in Fig. 12 using $L2$ error in the computed density, velocity, pressure, and temperature (L_∞ error shows similar trend). The user-specified constant $C_\kappa = 0.01$ is used in the LAD method. The eighth-order filtering scheme is introduced, and the results without the LAD method are also plotted. The linear least-square fits to the data at the three smallest grid spacings are constructed to provide the slopes, which are shown in parentheses. The initial interface is generated using Eq. (12), and a different smooth function $f_{\text{sm}} = (1 + \text{erf}[C_\delta \Delta R])/2$ is used with $C_\delta = 30.0$. Several grid spacings, $\Delta x = 0.00125$, 0.0025, 0.005, 0.01, 0.02, and 0.04, are used (note that the initial interface with $\Delta x = 0.01$ is almost identical to that with $C_\epsilon = 3.0$ used above). The order of accuracy of the present method with LAD method at the interface is estimated as being fourth-order accuracy with either the sixth- or the eighth-order filtering scheme. The result without the LAD method with the eighth-order filtering scheme achieves the formal order of accuracy of the sixth-order accuracy throughout the interface, whereas the order of accuracy is reduced with the sixth-order filtering scheme. The conventional scheme shows almost second-order accuracy, despite the formal order of accuracy being third-order accuracy, which is probably because of the limiter function. With $C_\kappa = 0.01$ and the present flow conditions, the overall order of accuracy of the method is considered to be fourth-order accuracy. The result also indicates that the order of the filtering scheme has a negligible effect on the accuracy at the interface when the LAD method is applied. Note that, as proved in Kawai and Lele [39], the formal order of accuracy (sixth-order) is retained in the regions where no interface exists.

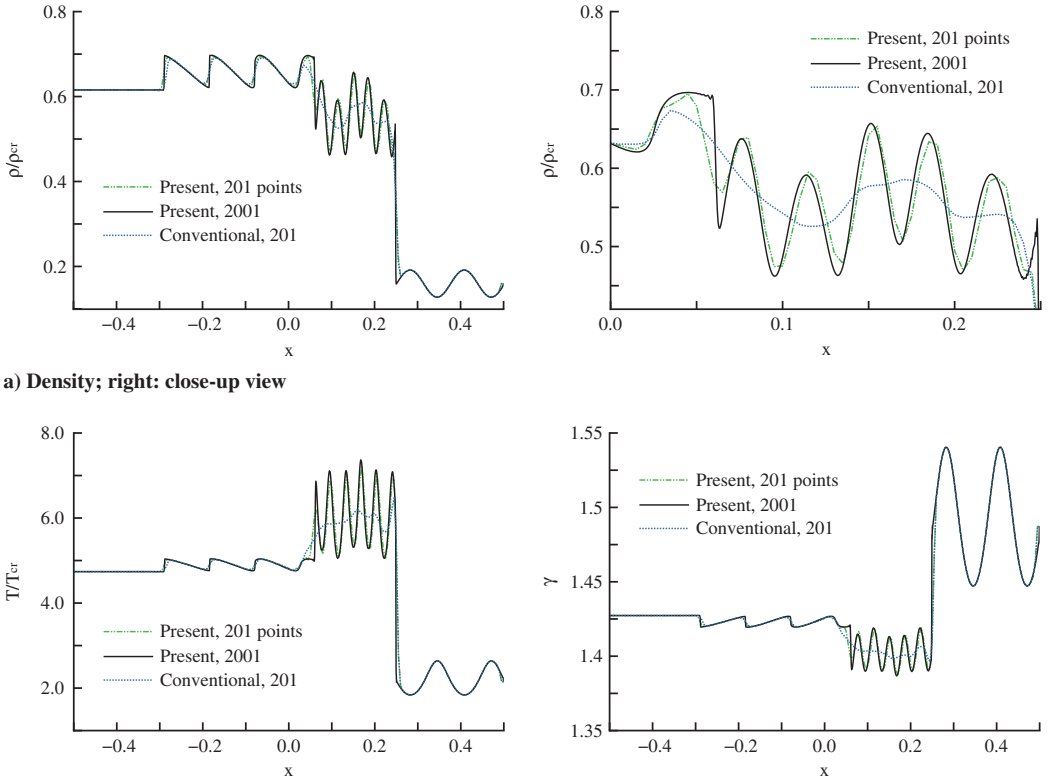

a) Density; right: close-up view

b) Temperature

c) Specific heat ratio

Fig. 14 Density, temperature, and specific heat ratio profiles of the present method compared with the conventional low-order scheme.

2. Shock Tube Problem

Simulations of a shock tube problem under a supercritical thermodynamic condition, introduced by Arina [55], are carried out as the second test case in which carbon dioxide is used as the working fluid. The critical temperature, pressure, and density of carbon dioxide are $T_{\mathrm{cr,CO_2}} = 304.22$ K, $p_{\mathrm{cr,CO_2}} = 7.37$ MPa, and $\rho_{\mathrm{cr,CO_2}} = 348.8$ kg/m^3 [43]. The initial conditions are

$$(\rho, u, p) = \begin{cases} (\rho_0, 0.0, 10p_0) & \text{if } 0 \le x \le 5 \text{ m}, \\ (0.01\rho_0, 0.0, 0.1p_0) & \text{if } 5 < x \le 10 \text{ m} \end{cases} \tag{14}$$

Here, $\rho_0 = \rho_{\mathrm{cr,CO_2}} = 348.8$ kg/m^3, and $p_0 = p_{\mathrm{cr,CO_2}} = 7.37$ MPa. 801 and 8001 grid points are used, and the solutions using 8001 grid points are used as the reference solutions. The smooth initial interface is generated with $C_\epsilon = 3.0$. The following results are at $t = 2.745 \times 10^{-3}$ s.

In the following two problems, the artificial bulk viscosity β^* is introduced because of the appearance of a shock wave. β^* is modeled using an user-specified constant $C_\beta = 1.75$ [21] as

$$\beta^* = C_\beta \rho \overline{\left| \sum_{l=1}^{n_d} \frac{\partial^r \nabla \cdot \boldsymbol{u}}{\partial \xi_l^r} \Delta \xi_l^r \Delta_l^2 \right|} \tag{15}$$

Figure 13 shows the density, velocity, and pressure profiles using 801 and 8001 grid points, where the results by the conventional low-order scheme (SHUS with MUSCL) and Arina [55] are also plotted for comparison. Arina used a conventional low-order scheme (AUSMDV with MUSCL) with the Redlich-Kwong equation of state. The smooth initial interface with $C_\epsilon = 3.0$ was applied to the conventional scheme (SHUS) as well as to the present result for consistency. The present result using 801 grid points is in good agreement with the reference solution and the results of the conventional schemes. No significant spurious oscillations are found in the profiles. The difference in shock position between the 801 and 8001 results is due to the difference of the initial interface thickness and the resultant shock speeds in the initial stage. The result obtained here demonstrates the applicability of the present method to supercritical flows with shock wave.

3. Modified Shu-Osher Problem

The Shu-Osher problem [56] has been widely used to assess the dissipation characteristics of numerical schemes. Here, the original Shu-Osher problem is extended to a supercritical thermodynamic condition. The working fluid is nitrogen, and the critical values are stated in the advection problem. The initial conditions are set as

$$(\rho, u, p) = \begin{cases} (3.857\rho_0, M_{\mathrm{ref}} c_{s,L}, 10.333p_0) & \text{if } -5 \le x \le -4 \text{ m}, \\ (\rho_0(1.0 + 0.2\sin 5x), 0.0, p_0) & \text{if } -4 < x \le 5 \text{ m} \end{cases} \tag{16}$$

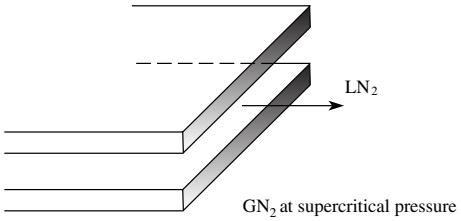

Fig. 15 Schematic of the 2-D planar jet computation.

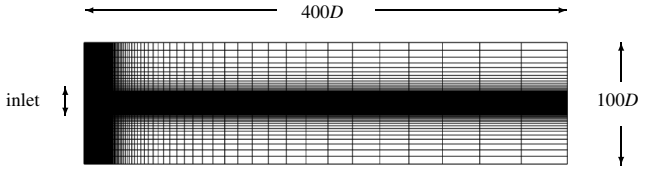

a) Whole view

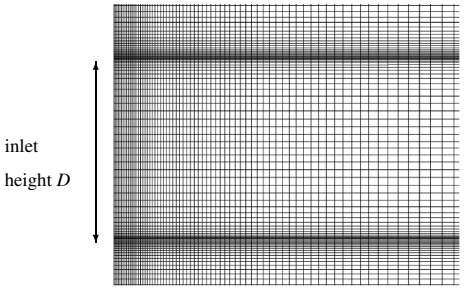

b) Close-up view near inlet

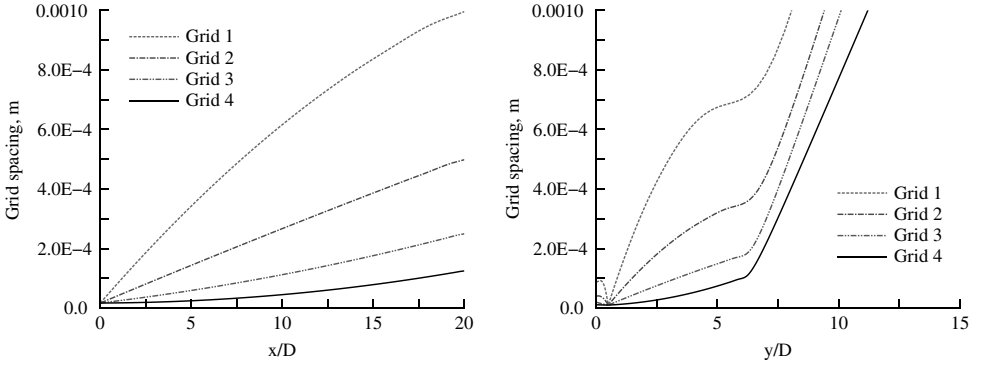

c) Distributions of grid spacing in streamwise (left) and normal (right) directions

Fig. 16 Computational grid: Grid 1 (195 × 185) and the distributions of grid spacing.

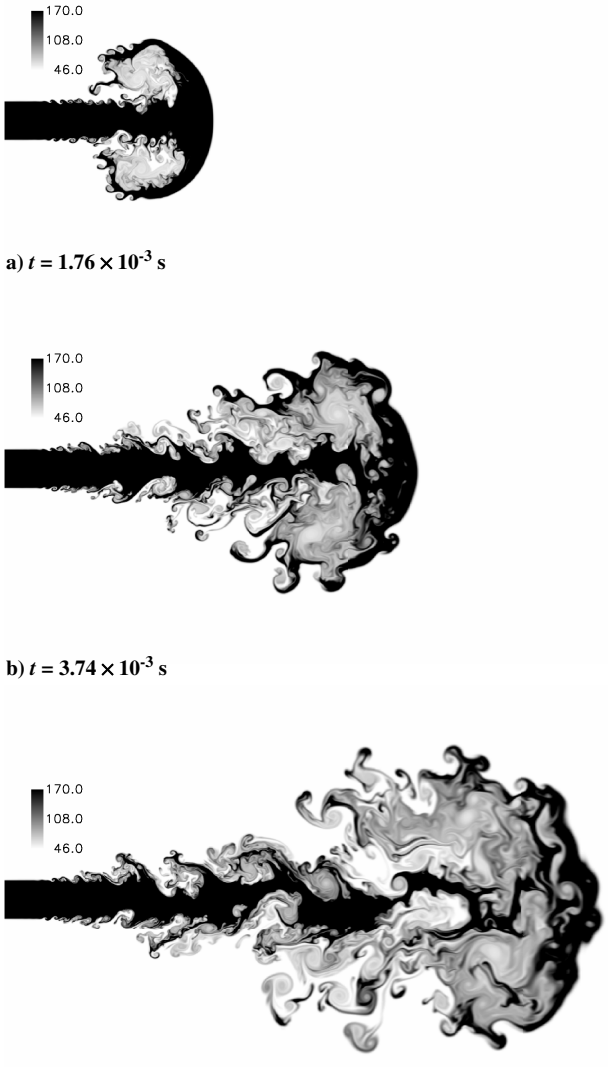

Fig. 17 A sequence of unsteady jet motion during the initial stage with the density field on Grid 4.

where $\rho_0 = 50.0$ kg/m^3, $p_0 = 4.0$ MPa, and $c_{s,L}$ is the sound speed in the left side. A supercritical thermodynamic condition (considering a typical combustion chamber condition as well as the advection problem) are first defined in the right side with the density fluctuation, and the left side states are determined such that the ratios of density and pressure and the shock speed (Mach number) correspond to those in the original Shu-Osher problem. Thus, the reference Mach number M_{ref} is estimated using the ideal gas speed of sound by $M_{\text{ref}} = u/\sqrt{\gamma p/\rho}$, where $u = 2.629$, $\gamma = 1.4$, $\rho = 3.857$, and $p = 10.333$. 201 grid points are used and 2001 grid points data are plotted as the reference solution. The initial interface is smoothened with $C_\epsilon = 3.0$. The following results are at $t = 5.903 \times 10^{-3}$ s.

Figure 14 shows the profiles of density, pressure, and the specific heat ratio. The present results using 201 grid points are in good agreement with the reference solutions, showing that the present method can resolve the high-frequency waves behind the shock wave with reasonable grid points (a small phase difference between the two results is due to the difference of the initial interface thickness). As shown in Fig. 14c, very small fluctuations of the specific heat ratio are also well-resolved, which may be preferable and important features for turbulence simulations in supercritical thermodynamic conditions. On the other hand, the conventional scheme cannot resolve such high-frequency waves because of the excessive dissipation characteristics. The present method has the capability to resolve high-frequency thermodynamic fluctuations, such as those of temperature or specific heat ratios under supercritical flow conditions with reasonable grid resolution.

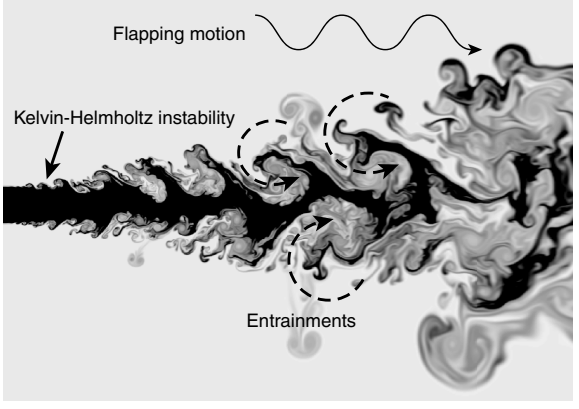

Fig. 18 Schematic of the unsteady flow structure of supercritical planar jet.

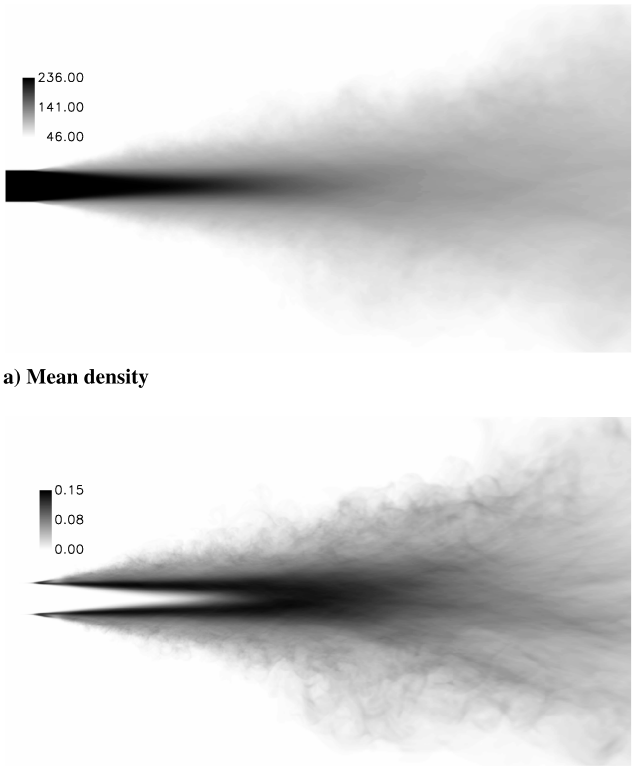

Fig. 19 Distributions of mean density and density fluctuation on Grid 4. $x/D = [0{:}20]$. The density fluctuation denotes $\rho'\rho'/\Delta\rho^2$, where $\Delta\rho = \rho_{\text{inj}} - \rho_{\text{cha}}$.

B. Two-Dimensional Viscous Flow Case: Low-Temperature Planar Jet Injected into Supercritical Pressure Condition

As an application to the multidimensional case, a 2-D planar viscous jet injected into a supercritical pressure condition is computed. A schematic and a computational grid are presented in Figs. 15 and 16, respectively. The computational conditions are based on general liquid rocket injector/chamber environments. The initial conditions are as follows:

$$(\rho, u, p, T) = \begin{cases} (236.3 \text{ kg/m}^3, 10.0 \text{ m/s}, 3.97 \text{ MPa}, 130.0 \text{ K}) & \text{for inlet,} \\ (45.46 \text{ kg/m}^3, 0.0 \text{ m/s}, 3.97 \text{ MPa}, 293.6 \text{ K}) & \text{for chamber} \end{cases} \tag{17}$$

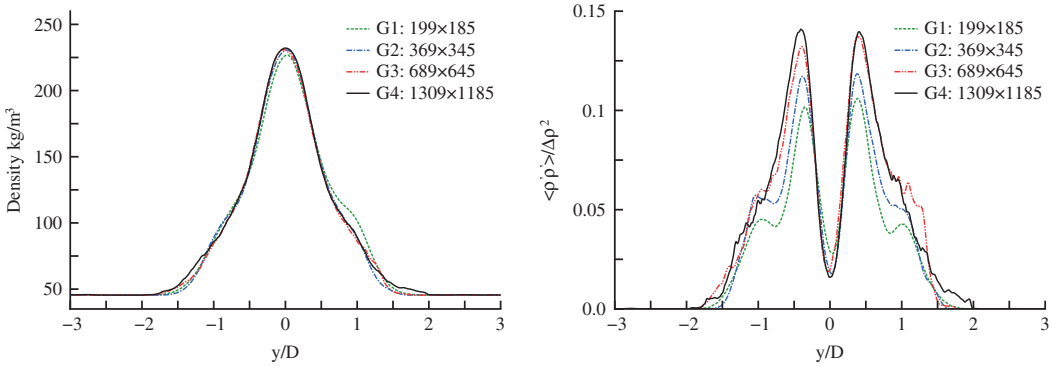

a) x/D = 5.0

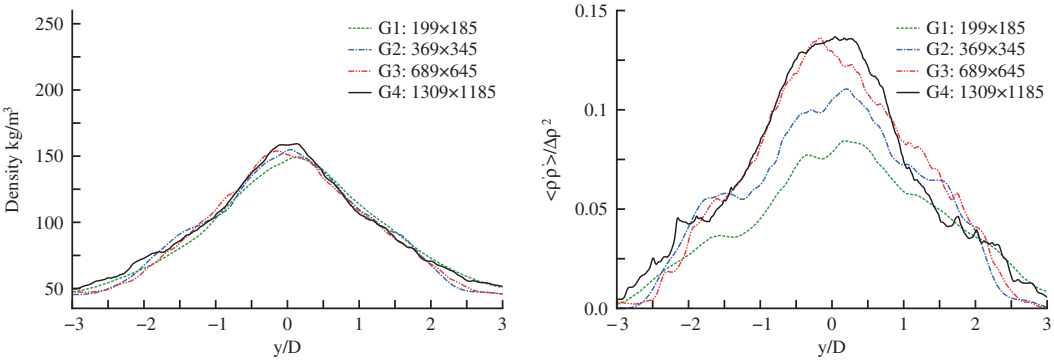

b) x/D = 10.0

Fig. 20 Mean and fluctuation density distributions with the effect of grid resolutions. $\Delta\rho = \rho_{inj} - \rho_{cha}$.

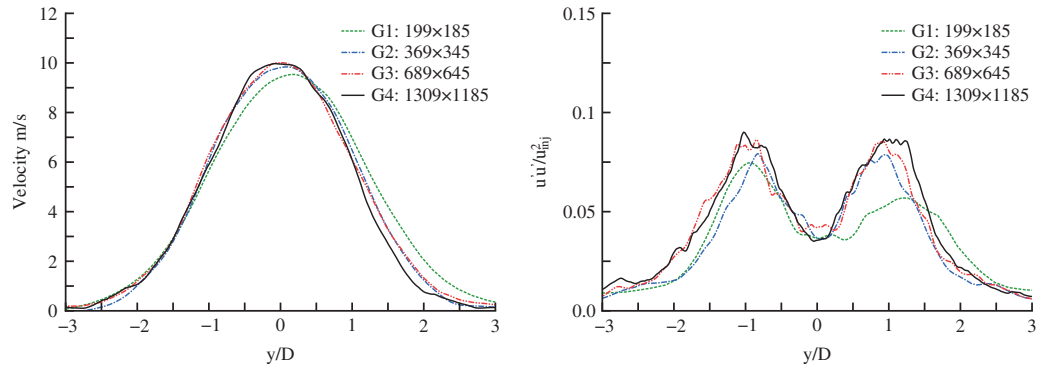

Fig. 21 Mean and fluctuation streamwise velocity distributions at $x/D = 10$ with the effect of grid resolutions.

Here, the density ratio ρ_{inj}/ρ_{cha} is 5.2, and the temperature ratio T_{inj}/T^* is 1.004, where T^* is the pseudo boiling-point temperature. The compressibility factor $p/\rho RT$ of the injected fluid is 0.4325. The velocity profile at the inlet is imposed using the hyperbolic tangent [57] :

$$u(y_c) = \frac{u_0}{2}\left\{1 + \tanh\left[0.25\frac{D}{\Theta}\left(\frac{D}{2y_c} - \frac{2y_c}{D}\right)\right]\right\} \qquad (18)$$

where D is the channel height, $u_0(=10$ m/s) the injection velocity, Θ is the momentum thickness, and y_c is the distance from the centerline. The slit height is $D = 2.2 \times 10^{-3}$ m, and the momentum thickness is taken to be $\Theta = D/60$ so that the initial velocity profile is properly resolved with any grids used. No perturbations are imposed in the velocity profile. The other variables (ρ, p) at the inlet are generated using Eq. (11) with $C_\epsilon = 3.0$. The jet Reynolds number is $Re \approx 1.48 \times 10^5$, based on D and u_0 and the Prandtl number $Pr \approx 7.5$. Four different grids (for which the number of grid point increases by approximately a factor of two in each direction) are performed: Grid 1 (195×185), Grid 2 (369×345), Grid 3 (689×645), and Grid 4 (1309×1185). The computational domain is $400D \times 100D$. Figure 16c presents the distributions of grid spacing in the streamwise and normal directions for each grid, in which the minimum grid spacing in the streamwise direction is

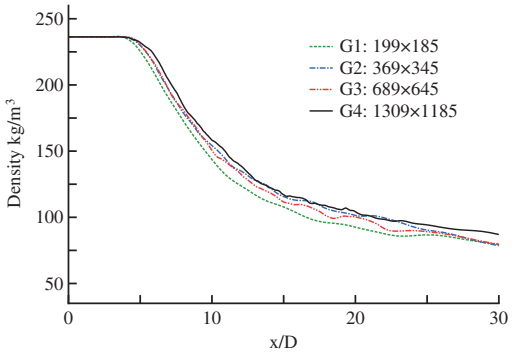

Fig. 22 Mean density profiles on the centerline with effect of grid resolutions.

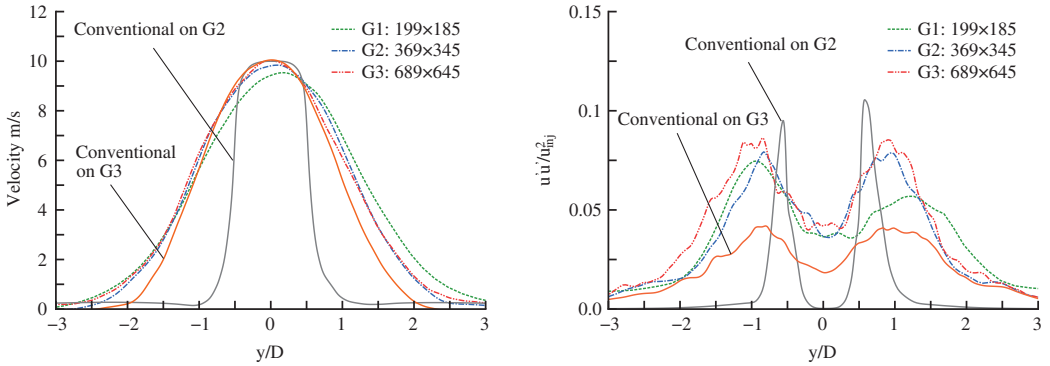

a) Mean and fluctuation streamwise velocity at $x/D = 10.0$

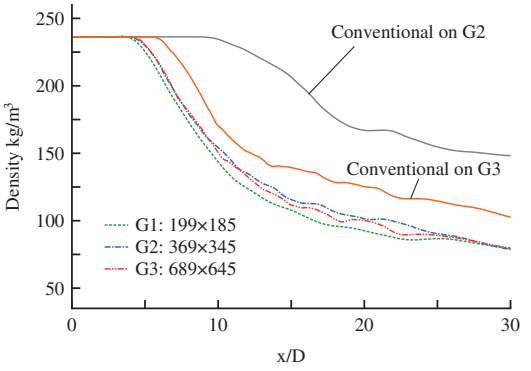

b) Mean density on the center line

Fig. 23 Comparisons between the present method and the conventional low-order scheme.

$\Delta s_{x,\min} = 1.75 \times 10^{-5}$ m at the inlet, and one in the normal direction is $\Delta s_{y,\min} = 1.0 \times 10^{-5}$ m at the center of shear layer. At the outlet, the pressure is fixed to the chamber pressure $p_{\text{out}} = 3.97$ MPa, and the other primitive variables are simply extrapolated. Slip wall is assumed at the upper and lower boundaries. The inviscid CFL number is fixed to 0.8. Statistical data that will be discussed are based on averaging flowfields over 60 ms after a 20 ms transient stage.

Figure 17 shows a sequence of the unsteady jet motion during the initial stage using the density field on Grid 4 (in which the maximum value of the contour range is lowered to clearly visualize the unsteady interface motions), and Fig. 18 highlights several important flow features. The present method successfully resolves several salient flow features of the jet mixing process, such as the Kelvin-Helmholtz instability, the small-scale vortical structure, the jet flapping motion, and the entrainment while retaining the interface-capturing capability.

Figure 19 shows the distributions of the mean and fluctuation density on Grid 4. The jet core region is recognized in the mean density distribution, and the fluctuations are produced mainly in the shear layer and in the transition zone downstream of the jet core

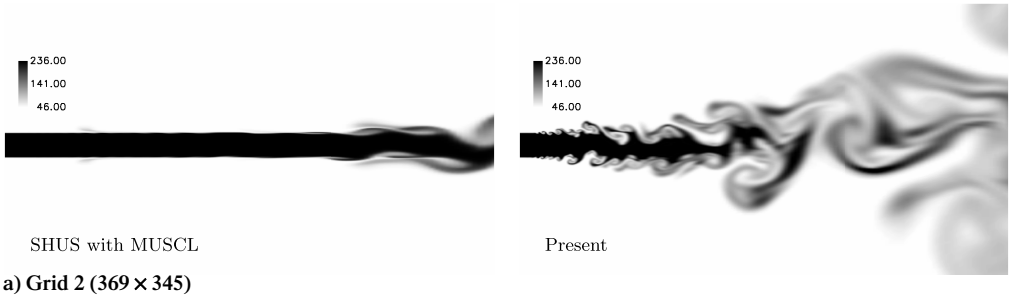

a) Grid 2 (369 × 345)

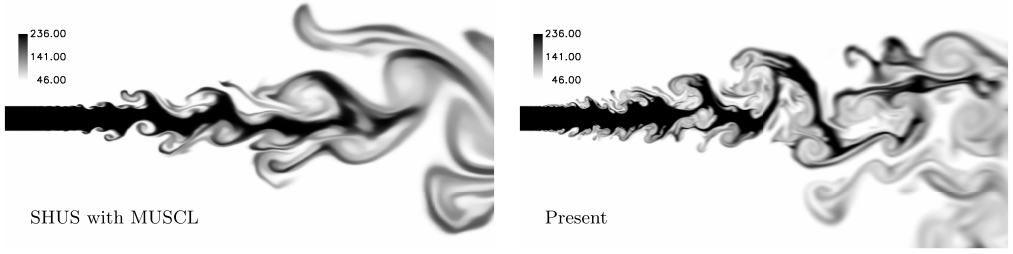

b) Grid 3 (689 × 645)

Fig. 24 Comparison between the present method and the conventional low-order scheme on density distributions at $t = 0.03$ s, showing the effect of grid resolution: $x/D = [0{:}20]$.

where the flapping motion begins to occur. Figure 20 presents the mean and fluctuation density at $x/D = 5.0$ and $x/D = 10.0$ with different grid resolutions. An almost identical result is obtained for the mean profile over the four grid resolutions, and the fluctuation shows a trend toward grid convergence. The results are almost grid-converged on Grid 3. The streamwise velocity in Fig. 21 also shows a similar feature. Moreover, the mean density profile on the centerline, as shown in Fig. 22, presents the grid-converged solution. Therefore, the present result on Grids 3 and 4 could be considered to closely represent a two-dimensional DNS solution.

Finally, comparisons with the conventional scheme (SHUS with MUSCL) are made in Fig. 23 using the mean and fluctuation streamwise velocity at $x/D = 10$ and the mean density on the centerline. The results clearly show the superiority of the present method in resolving both the mean and fluctuation quantities. The present method, even with Grid 1, shows much better performance in resolving the mean and fluctuation quantities compared with the conventional scheme with Grids 2 and 3. With the conventional scheme, the shear layer grows little because of the excessive numerical dissipation, by which the flow unsteadiness and the small-scale vortex generation are suppressed, resulting in the longer dense-core (see Fig. 23b). The conventional scheme needs much finer grid resolution to reach the converged-solution. Figure 24 shows a qualitative comparison of instantaneous density distributions between the present and the conventional schemes on Grids 2 and 3. Unsteady vortical structures are not greatly produced with the conventional scheme on Grid 2; on the other hand, the present method resolves relatively smaller-scale vortices generated from further upstream of the jet on the same grid resolution. It should be noted that some computations without the limiter function using the conventional low-order scheme failed because of the unphysical over/undershoot produced near the interface, thus indicating that some interface-capturing methodology is required to simulate flows involving large density/temperature gradients in supercritical pressure conditions even when conventional low-order schemes are applied.

IV. Conclusion

A high-resolution numerical method for flows under supercritical thermodynamic conditions has been presented. The present method is based on the sixth-order compact differencing scheme to resolve a wide range of flow scales. The LAD method is used to numerically capture the large density/temperature gradients at the interfaces and the shock wave.

The results for the advection problem showed that the present method can be successfully applied to super/transcritical flows with large density/temperature gradients without any significant spurious oscillations. The artificial thermal conductivity using the derivative of temperature successfully suppresses the numerical instabilities at the interfaces while minimizing the impact on the solutions. The smooth initial interface also works to eliminate the numerical instability occurring in the initial stage. The overall order of accuracy of the present method was estimated as being fourth-order accuracy in the interface advection problem with either the sixth- or the eight-order filtering scheme. In the shock tube problem, the present results showed good agreement with a previous computational study, demonstrating its capability of simulating a shock wave under the supercritical condition. The modified Shu-Osher problem demonstrated the superiority and low dissipation characteristics of the present method in resolving high-frequency fluctuations as compared with the conventional low-order scheme. The results for the 2-D low-temperature planar jet simulations showed the applicability of the present method to multidimensional problems and its ability to resolve the unsteady complicated jet structures under supercritical pressure conditions with reasonable grid resolutions.

Appendix A: Derivation of Thermodynamic Properties

Although a derivation of thermodynamic relations under supercritical conditions was provided in an earlier study [5], it might be useful to provide a consistent formulation for the present method in this paper. As a result, the whole process of supercritical flow simulations can be clearly understood, the implementation should be easier, and the paper can stand alone. Moreover, the thermodynamic relationship is key to supercritical flow computations.

We start with an equation in which the internal energy is defined as a function of the temperature and specific volume:

$$e(T,\rho) = \int \left(\frac{\partial e}{\partial T}\right)_V \mathrm{d}T + \int \left(\frac{\partial e}{\partial V}\right)_T \mathrm{d}V \tag{A1}$$

and using the relations $(\frac{\partial e}{\partial T})_V = C_v$ for the heat capacity at constant volume, Eq. (A1) is written as

$$e(T,\rho) = \int C_v \,\mathrm{d}T + \int \left(\frac{\partial e}{\partial V}\right)_T \mathrm{d}V = e_0(T) + \int \left(\frac{\partial e}{\partial V}\right)_T \mathrm{d}V \tag{A2}$$

where $\int C_v \,\mathrm{d}T = e_0(T) = C_v T$ taken in this study (while C_v may be approximated by a polynomial equation of temperature).

Consider the second term on the right hand in Eq. (A2). The two thermodynamic relations first given are

$$\mathrm{d}\,e = T\,\mathrm{d}S - p\,\mathrm{d}V \tag{A3}$$

$$\mathrm{d}\,e = \frac{\partial e}{\partial T}\,\mathrm{d}T + \frac{\partial e}{\partial V}\,\mathrm{d}V = 0 + \frac{\partial e}{\partial V}\,\mathrm{d}V \tag{A4}$$

and they follow that

$$\frac{\partial e}{\partial V}\,\mathrm{d}V = T\,\mathrm{d}S - p\,\mathrm{d}V \tag{A5}$$

Equation (A5) is then written as

$$\left(\frac{\partial e}{\partial V}\right)_T = T\left(\frac{\partial S}{\partial V}\right)_T - p = T\left(\frac{\partial p}{\partial T}\right)_V - p \tag{A6}$$

where the relation $(\frac{\partial S}{\partial V})_T = (\frac{\partial p}{\partial T})_V$ is used, which is derived from a thermodynamic relation, $\mathrm{d}F = -S\,\mathrm{d}T - p\,\mathrm{d}V$, where F is the Helmholtz free energy. The second term in Eq. (A2) is therefore given as

$$\int \left(\frac{\partial e}{\partial V}\right)_T \mathrm{d}V = \int_\infty^V \left[T\left(\frac{\partial p}{\partial T}\right)_V - p\right]_T \mathrm{d}V \tag{A7}$$

and this appears in Eq. (6).

For the SRK equation of state (Eq. (5)), the derivative $(\frac{\partial p}{\partial T})_V$ in Eq. (A7) becomes

$$\left(\frac{\partial p}{\partial T}\right)_V = \frac{R}{V-b} - \frac{a\frac{\partial \alpha}{\partial T}}{V^2 + bV} \tag{A8}$$

where α and $\frac{\partial \alpha}{\partial T}$ are

$$\alpha = [1 + f(\omega)(1 - (T/T_c)^{0.5})]^2 \tag{A9}$$

$$\frac{\partial \alpha}{\partial T} = -f(\omega)[1 + f(\omega)(1 - (T/T_c)^{0.5})](TT_c)^{-0.5} \tag{A10}$$

Here, $f(\omega)$ is expressed as $f(\omega) = 0.480 + 1.574\omega - 0.176\omega^2$, where ω is the acentric factor. Substituting Eq. (A8) into Eq. (A7), we obtain

$$\begin{aligned}\int_\infty^V \left[T\left(\frac{\partial p}{\partial T}\right)_V - p\right]_T \mathrm{d}V &= \int_\infty^V a\frac{\alpha - T\frac{\partial \alpha}{\partial T}}{V^2 + bV}\,\mathrm{d}V \\ &= a\left(\alpha - T\frac{\partial \alpha}{\partial T}\right)\frac{1}{b}\int_\infty^V \left(\frac{1}{V} - \frac{1}{V+b}\right)\mathrm{d}V\end{aligned} \tag{A11}$$

Eq. (A11) becomes

$$\int_{\infty}^{V}\left[T\left(\frac{\partial p}{\partial T}\right)_V - p\right]_T \mathrm{d}V = a\left(\alpha - T\frac{\partial \alpha}{\partial T}\right)\frac{1}{b}\log_e\left|\frac{V}{V+b}\right| \quad \text{(A12)}$$

and the internal energy is finally given from Eq. (A2) as

$$e(T,\rho) = e_0(T) + a\left(\alpha - T\frac{\partial \alpha}{\partial T}\right)\frac{1}{b}\log_e\left|\frac{V}{V+b}\right| \quad \text{(A13)}$$

The temperature is obtained from Eq. (A13), provided the density and the internal energy are known. Generally, Eq. (A13) can be solved using an iterative method, such as the Newton-Raphson method. Solutions from the van der Waals equation of state are used for the initial guess in this study. The pressure is calculated using Eq. (5).

Appendix B: Spatial Derivatives and Filtering

I. Compact Differencing and Filtering Schemes

The governing Eqs. (1–3) are solved in the strong conservative form and in generalized curvilinear coordinates, where the spatial derivatives at node i are computed according to the sixth-order compact scheme [32]:

$$\alpha\frac{\partial f_{i-1}}{\partial \xi} + \frac{\partial f_i}{\partial \xi} + \alpha\frac{\partial f_{i+1}}{\partial \xi} = a\frac{f_{i+1}-f_{i-1}}{2\Delta\xi} + b\frac{f_{i+2}-f_{i-2}}{4\Delta\xi} \quad \text{(B1)}$$

where $\alpha = \frac{1}{3}$, $a = \frac{14}{9}$, and $b = \frac{1}{9}$. At boundary points $i = 1$ and 2 and, correspondingly, at $i = i\max - 1$ and $i\max$, second- and fourth-order one-sided formulas are used that retain the tridiagonal form of the equation set [34]. A sixth-order low-pass spatial filtering is

$$\alpha_f\hat{f}_{i-1} + \hat{f}_i + \alpha_f\hat{f}_{i+1} = \sum_{n=0}^{3}\frac{a_n}{2}(f_{i+n} + f_{i-n}) \quad \text{(B2)}$$

where $\hat{f}$ is the filtered variable and $a_0 = \frac{11+10\alpha_f}{16}$, $a_1 = \frac{15+34\alpha_f}{32}$, $a_2 = \frac{-3+6\alpha_f}{16}$, and $a_3 = \frac{1-2\alpha_f}{32}$. α_f is a free parameter satisfying the inequality $-0.5 < \alpha_f \leq 0.5$. High-order one-sided formulas are used for the near boundary points at $i = 1$–4 and, correspondingly, at $i = i\max - 3$ to $i\max$ [34].

II. LAD method

The fourth derivative term in Eq. (10) is evaluated using a fourth-order central differencing scheme

$$\frac{\partial^4 f_i}{\partial \xi_l^4} = b\frac{f_{i+3} - 9f_{i+1} + 16f_i - 9f_{i-1} + f_{i-3}}{6\Delta\xi_l^4} + a\frac{f_{i+2} - 4f_{i+1} + 6f_i - 4f_{i-1} + f_{i-2}}{\Delta\xi_l^4} \quad \text{(B3)}$$

where $a = 2$ and $b = -1$. At boundary points $i = 1, 2, i\max - 1$, and $i\max$, a one-sided second-order explicit scheme is used and at $i = 3$, and at $i\max - 2$, a second-order central scheme is used [39]. The over-bar in Eq. (10) denotes a truncated-Gaussian filter [36], expressed as

$$\bar{f}_i = \frac{3565}{10368}f_i + \frac{3091}{12960}(f_{i-1} + f_{i+1}) + \frac{1997}{25920}(f_{i-2} + f_{i+2}) + \frac{149}{12960}(f_{i-3} + f_{i+3}) + \frac{107}{103680}(f_{i-4} + f_{i+4}) \quad \text{(B4)}$$

At boundary points 1–4 and $i\max - 3$ to $i\max$, the value f_i is mirrored across the boundary in order to apply Eq. (B4).

Acknowledgments

This research was supported by Japan Aerospace Exploration Agency aerospace project research fellowship. We are grateful to several collaborators at the Rocket Engine Modeling Laboratory in the University of Tokyo, in particular, Shin-ichi Tsuda for various discussions about thermodynamic fluid properties and Hideyo Negishi for discussions about supercritical jet flows.

References

[1] Yang, V., Habiballah, M., Hulka, J., and Popp, M., *Liquid Rocket Thrust Chambers: Aspects of Modeling, Analysis, and Design*, Progress in Astronautics and Aeronautics, 200, American Institute of Aeronautics and Astronautics, Inc., Reston, VA, 2004.

[2] Mayer, W., and Tamura, H., "Propellant Injection in a Liquid Oxygen/Gaseous Hydrogen Rocket Engine," *Journal of Propulsion and Power*, Vol. 12, No. 6, 1996, pp. 1137–1147. doi:10.2514/3.24154

[3] Chehroudi, B., Talley, D., and Coy, E., "Visual Characteristics and Initial Growth Rates of Round Cryogenic Jets at Subcritical and Supercritical Pressures," *Physics of Fluids*, Vol. 14, No. 2, 2002, pp. 850–861. doi:10.1063/1.1430735

[4] Oefelein, J., and Yang, V., "Modeling High-Pressure Mixing and Combustion Processes in Liquid Rocket Engines," *Journal of Propulsion and Power*, Vol. 14, No. 5, 1998, pp. 843–857. doi:10.2514/2.5349

[5] Meng, H., and Yang, V., "A Unified Treatment of General Fluid Thermodynamics and its Application to a Preconditioning Scheme," *Journal of Computational Physics*, Vol. 189, No. 1, 2003, pp. 277–304. doi:10.1016/S0021-9991(03)00211-0

[6] Zong, N., Meng, H., Hsieh, S., and Yang, V., "A Numerical Study of Cryogenic Fluid Injection and Mixing Under Supercritical Conditions," *Physics of Fluids*, Vol. 16, No. 12, 2004, pp. 4248–4261. doi:10.1063/1.1795011

[7] Zong, N., and Yang, V., "Cryogenic Fluid Jets and Mixing Layers in Transcritical and Supercritical Environments," *Combustion Science and Technology*, Vol. 178, No. 1, 2006, pp. 193–227. doi:10.1080/00102200500287613

[8] Hosangadi, A., Lee, C., Kannepalli, C., and Arunajatesan, S., "Three-Dimensional Hybrid RANS/LES Simulations of a Supercritical Liquid Nitrogen Jet," AIAA Paper 2008-5227, 2008.

[9] Schmitt, T., Selle, L., Ruiz, A., and Cuenot, B., "Large-Eddy Simulation of Supercritical Pressure Round Jets," *AIAA Journal*, Vol. 48, No. 9, 2010, pp. 2133–2144. doi:10.2514/1.J050288

[10] Branam, R., and Mayer, W., "Characterization of Cryogenic Injection at Supercritical Pressure," *Journal of Propulsion and Power*, Vol. 19, No. 3, 2003, pp. 342–355. doi:10.2514/2.6138

[11] Cutrone, L., Battista, F., Ranuzzi, G., Bonifacio, S., and Steelant, J., "A CFD Method for Simulation of Mixing and Combustion in High-Pressure LO_x/Methane Rocket Engines," AIAA Paper 2008-949, 2008.

[12] Bellan, J., "Supercritical (and Subcritical) Fluid Behavior and Modeling: Drops, Streams, Shear and Mixing Layers, Jets, and Sprays," *Progress in Energy and Combustion Science*, Vol. 26, No. 4–6, 2000, pp. 329–366. doi:10.1016/S0360-1285(00)00008-3

[13] Miller, R., Harstad, K., and Bellan, J., "Direct Numerical Simulations of Supercritical Fluid Mixing Layers Applied to Heptane–Nitrogen," *Journal of Fluid Mechanics*, Vol. 436, 2001, pp. 1–39.

[14] Okong'o, N., and Bellan, J., "Small-Scale Dissipation in Supercritical, Transitional, Mixing Layers," AIAA Paper 2009-807, 2009.

[15] Selle, L., Okong'o, N., Bellan, J., and Harstad, K., "Modelling of Subgrid-Scale Phenomena in Supercritical Transitional Mixing Layers: an a Priori Study," *Journal of Fluid Mechanics*, Vol. 593, 2007, pp. 57–91.

[16] Taskinoglu, E., and Bellan, J., "An a Posteriori Study of a DNS Database Describing Supercritical Binary-Species Mixing," AIAA Paper 2009-808, 2009.

[17] Selle, L., and Schmitt, T., "Large-Eddy Simulation of Single-Species Flows Under Supercritical Thermodynamic Conditions," *Combustion Science and Technology*, Vol. 182, No. 4, 2010, pp. 392–404. doi:10.1080/00102200903462664

[18] Yang, V., "Modeling of Supercritical Vaporization, Mixing, and Combustion Processes in Liquid-Fueled Propulsion Systems," *Proceedings of the Combustion Institute*, Vol. 28, No. 1, 2000, pp. 925–942. doi:10.1016/S0082-0784(00)80299-4

[19] Larsson, J., Lele, S., and Moin, P., *Effect of Numerical Dissipation on the Predicted Spectra for Compressible Turbulence*, Annual Research Briefs, Center for Turbulence Research, Stanford University, Stanford, CA, 2007, pp. 47–57.

[20] Johnsen, E., Larsson, J., Bhagatwala, A., Cabot, W., Moin, P., Olson, B., Rawat, P., Shankar, S., Sjogreen, B., Yee, H., Zhong, X., Lele, S., "Assessment of High-Resolution Methods for Numerical Simulations of Compressible Turbulence with Shock Waves," *Journal of Computational Physics*, Vol. 229, No. 4, 2010, pp. 1213–1237. doi:10.1016/j.jcp.2009.10.028

[21] Kawai, S., Shankar, S., and Lele, S., "Assessment of Localized Artificial Diffusivity Scheme for Large-Eddy Simulation of Compressible Turbulent Flows," *Journal of Computational Physics*, Vol. 229, No. 5, 2010, pp. 1739–1762. doi:10.1016/j.jcp.2009.11.005

[22] Jiang, G., and Shu, C., "Efficient Implementation of Weighted ENO Schemes," *Journal of Computational Physics*, Vol. 126, No. 1, 1996, pp. 202–228. doi:10.1006/jcph.1996.0130

[23] Pirozzoli, S., "Numerical Methods for High-Speed Flows," *Annual Review of Fluid Mechanics*, Vol. 43, No. 1, 2011.163–194. doi:10.1146/annurev-fluid-122109-160718

[24] Kawai, S., and Terashima, H., "A High-Resolution Scheme for Compressible Multicomponent Flows with Shock Waves," *International Journal for Numerical Methods in Fluids*, Vol. 66, No. 10, 2011, pp. 1207–1225. doi:10.1002/fld.2306

[25] Mayer, W., Telaar, J., Branam, R., Schneider, G., and Hussong, J., "Raman Measurements of Cryogenic Injection at Supercritical Pressure," *Heat and Mass Transfer*, Vol. 39, No. 8, 2003, pp. 709–719. doi:10.1007/s00231-002-0315-x

[26] Yin, Y., and Lu, X., "Effects of Injection Temperature on the Jet Evolution Under Supercritical Conditions," *Chinese Science Bulletin*, Vol. 54, No. 22, 2009, pp. 4197–4204. doi:10.1007/s11434-009-0626-0

[27] Soave, G., "Equilibrium Constants from a Modified Redlich-Kwong Equation of State," *Chemical Engineering Science*, Vol. 27, No. 6, 1972, pp. 1197–1203. doi:10.1016/0009-2509(72)80096-4

[28] Benedict, M., Webb, G. B., and Rubin, L. C., "An Empirical Equation for Thermodynamic Properties of Light Hydrocarbons and Their Mixtures: I. Methane, Ethane, Propane, and n-Butane," *Journal of Chemical Physics*, Vol. 8, No. 4, 1940, p. 334–345. doi:10.1063/1.1750658

[29] Poling, B. E., Prausnitz, J. M., and O'Connell, J. P., *The Properties of Gases and Liquids*, 5th ed., McGaw-Hill, New York, 2000.

[30] Zeberg-Mikkelsen, C., Quinones-Cisneros, S., and Stenby, E., "Viscosity Modeling of Light Gases at Supercritical Conditions Using the Friction Theory," *Industrial and Engineering Chemistry Research*, Vol. 40, No. 17, 2001, pp. 3848–3854. doi:10.1021/ie000987d

[31] Vasserman, A., and Nedostup, V., "An Equation for Calculation of the Thermal Conductivity of Gases and Liquids," *Journal of Engineering Physics and Thermophysics*, Vol. 20, No. 1, 1971, pp. 89–92. 10.1007/BF00868593

[32] Lele, S., "Compact Finite Difference Schemes with Spectral-like Resolution," *Journal of Computational Physics*, Vol. 103, No. 1, 1992, pp. 16–42. doi:10.1016/0021-9991(92)90324-R

[33] Gottlieb, S., and Shu, C., "Total Variation Diminishing Runge-Kutta Schemes," *Mathematics of Computation*, Vol. 67, No. 221, 1998, pp. 73–85. doi:10.1090/S0025-5718-98-00913-2

[34] Gaitonde, D., and Visbal, M., "Pade-Type Higher-Order Boundary Filters for the Navier-Stokes Equations," *AIAA Journal*, Vol. 38, No. 11, 2000, pp. 2103–2112. doi:10.2514/2.872

[35] Jameson, A., Schmidt, W., and Turkel, E., "Numerical Solutions of the Euler Equations by Finite Volume Methods with Runge-Kutta Time Stepping Schemes," AIAA Paper 81-1259, 1981.

[36] Cook, A., and Cabot, W., "A High-Wavenumber Viscosity for High-Resolution Numerical Methods," *Journal of Computational Physics*, Vol. 195, No. 2, 2004, pp. 594–601. doi:10.1016/j.jcp.2003.10.012

[37] Cook, A., "Artificial Fluid Properties for Large-Eddy Simulation of Compressible Turbulent Mixing," *Physics of Fluids*, Vol. 19, No. 5, 2007, p. 055103. doi:10.1063/1.2728937

[38] Cook, A., "Enthalpy Diffusion in Multicomponent Flows," *Physics of Fluids*, Vol. 21, No. 5, 2009, p. 055109. doi:10.1063/1.3139305

[39] Kawai, S., and Lele, S., "Localized Artificial Diffusivity Scheme for Discontinuity Capturing on Curvilinear Meshes," *Journal of Computational Physics*, Vol. 227, No. 22, 2008, pp. 9498–9526. doi:10.1016/j.jcp.2008.06.034

[40] Lee, S., Lele, S., and Moin, P., "Interaction of Isotropic Turbulence with Shock Waves: Effect of Shock Strength," *Journal of Fluid Mechanics*, Vol. 340, No. 1, 1997, pp. 225–247. doi:10.1017/S0022112097005107

[41] Visbal, M., and Gaitonde, D., "Shock Capturing Using Compact-Differencing-Based Methods," AIAA Paper 2005-1265, 2005.

[42] Arora, M., and Roe, P., "On Postshock Oscillations Due to Shock Capturing Schemes in Unsteady Flows," *Journal of Computational Physics*, Vol. 130, No. 1, 1997, pp. 25–40. doi:10.1006/jcph.1996.5534

[43] Lemmon, E., Huber, M., and McLinden, M., "NIST Standard Reference Database 23: Reference Fluid Thermodynamic and Transport Properties-REFPROP, Version 8.0," National Institute of Standards and Technology, Standard Reference Data Program, Gaithersburg, MD, 2007.

[44] Cheng, G., and Farmer, R., "Real Fluid Modeling of Multiphase Flows in Liquid Rocket Engine Combustors," *Journal of Propulsion and Power*, Vol. 22, No. 6, 2006, pp. 1373–1381. doi:10.2514/1.17272

[45] Kawai, S., and Fujii, K., "Compact Scheme with Filtering for Large-Eddy Simulation of Transitional Boundary Layer," *AIAA Journal*, Vol. 46, No. 3, 2008, pp. 690–700. doi:10.2514/1.32239

[46] Shukla, R., Pantano, C., and Freund, J., "An Interface Capturing Method for the Simulation of Multi-Phase Compressible Flows," *Journal of Computational Physics*, Vol. 229, No. 19, 2010, pp. 7411–7439. doi:10.1016/j.jcp.2010.06.025

[47] Saurel, R., and Abgrall, R., "A Simple Method for Compressible Multifluid Flows," *SIAM Journal on Scientific Computing*, Vol. 21, No. 3, 1999, pp. 1115–1145. doi:10.1137/S1064827597323749

[48] Chang, C., and Liou, M., "A Robust and Accurate Approach to Computing Compressible Multiphase Flow: Stratified Flow Model and AUSM+-Up Scheme," *Journal of Computational Physics*, Vol. 225, No. 1, 2007, pp. 840–873. doi:10.1016/j.jcp.2007.01.007

[49] Shima, E., and Jounouchi, T., "Role of CFD in Aeronautical Engineering (No. 14)-AUSM type Upwind Schemes," *Proceedings of the 14th NAL Symposium on Aircraft Computational Aerodynamics*, NAL-SP34, National Aerospace Laboratory, Tokyo, 1997, pp. 7–12.

[50] Liou, M., and Steffen, C., "A New Flux Splitting Scheme," *Journal of Computational Physics*, Vol. 107, No. 1, 1993, pp. 23–39. doi:10.1006/jcph.1993.1122

[51] van Leer, B., "Towards the Ultimate Conservative Difference Scheme. IV. A New Approach to Numerical Convection," *Journal of Computational Physics*, Vol. 23, No. 3, 1977, pp. 276–299. doi:10.1016/0021-9991(77)90095-X

[52] van Leer, B., "Towards the Ultimate Conservative Difference Scheme. V. A Second-Order Sequel to Godunov's Method," *Journal of Computational Physics*, Vol. 32, No. 1, 1979, pp. 101–136. doi:10.1016/0021-9991(79)90145-1

[53] van Albada, G., van Leer, B., and Roberts, W., Jr, "A Comparative Study of Computational Methods in Cosmic Gas Dynamics," *Astronomy and Astrophysics*, Vol. 108, No. 1, 1982, pp. 76–84.

[54] Abgrall, R., and Karni, S., "Computations of Compressible Multifluids," *Journal of Computational Physics*, Vol. 169, No. 2, 2001, pp. 594–623. doi:10.1006/jcph.2000.6685

[55] Arina, R., "Numerical Simulation of Near-Critical Fluids," *Applied Numerical Mathematics*, Vol. 51, No. 4, 2004, pp. 409–426. doi:10.1016/j.apnum.2004.06.002

[56] Shu, C., and Osher, S., "Efficient Implementation of Essentially Non-Oscillatory Shock-Capturing Schemes, II," *Journal of Computational Physics*, Vol. 83, No. 1, 1989, pp. 32–78. doi:10.1016/0021-9991(89)90222-2

[57] Hilgers, A., *Control and Optimization of Turbulent Jet Mixing*, Annual Research Briefs, Center for Turbulence Research, Stanford University, Stanford, CA, 2000, pp. 45–54.

S. Fu
Associate Editor